scientific reports

Check for updates

OPEN

Investigation of molecular mechanisms of experimental compounds in murine models of chronic allergic airways disease using synchrotron Fourier-transform infrared microspectroscopy

Nadia Mazarakis[1,2,3], Jitraporn Vongsvivut[4], Keith R. Bambery[4], Katherine Ververis[1], Mark J. Tobin[4], Simon G. Royce[6], Chrishan S. Samuel[6], Kenneth J. Snibson[2], Paul V. Licciardi[3,5] & Tom C. Karagiannis[1,7]✉

The ovalbumin-induced (OVA) chronic allergic airways murine model is a well-established model for investigating pre-clinical therapies for chronic allergic airways diseases, such as asthma. Here, we examined the effects of several experimental compounds with potential anti-asthmatic effects including resveratrol (RV), relaxin (RLN), L-sulforaphane (LSF), valproic acid (VPA), and trichostatin A (TSA) using both a prevention and reversal model of chronic allergic airways disease. We undertook a novel analytical approach using focal plane array (FPA) and synchrotron Fourier-transform infrared (S-FTIR) microspectroscopic techniques to provide new insights into the mechanisms of action of these experimental compounds. Apart from the typical biological effects, S-FTIR microspectroscopy was able to detect changes in nucleic acids and protein acetylation. Further, we validated the reduction in collagen deposition induced by each experimental compound evaluated. Although this has previously been observed with conventional histological methods, the S-FTIR technique has the advantage of allowing identification of the type of collagen present. More generally, our findings highlight the potential utility of S-FTIR and FPA-FTIR imaging techniques in enabling a better mechanistic understanding of novel asthma therapeutics.

Animal models designed specifically for chronic lung diseases such as asthma are important for investigating the underlying mechanisms of the disease and the effectiveness of potential novel therapies[1]. One of the most widely used models for asthma is the mouse chronic allergic airways disease model that utilises ovalbumin (OVA)[2,3]. This model recapitulates many of the hallmark characteristics of chronic asthma including eosinophilic inflammation, airway hyperresponsiveness, epithelial wall thickening, goblet cell metaplasia, and fibrosis[4,5].

Current therapies for people with asthma include bronchial dilators, glucocorticosteroids that target inflammation, or a combination of these. However, they have limitations, particularly for patients with severe asthma

[1]Epigenomic Medicine Laboratory, Department of Diabetes, Central Clinical School, Monash University, Alfred Centre, 99 Commercial Road, Melbourne, VIC 3004, Australia. [2]Faculty of Veterinary and Agricultural Sciences, University of Melbourne, Parkville, VIC 3010, Australia. [3]Murdoch Children's Research Institute, Melbourne, VIC 3004, Australia. [4]ANSTO Australian Synchrotron, Clayton, VIC 3168, Australia. [5]Department of Paediatrics, University of Melbourne, Parkville, VIC 3010, Australia. [6]Department of Pharmacology, Monash Biomedicine Discovery Institute, Monash University, Clayton, VIC 3168, Australia. [7]Department of Clinical Pathology, University of Melbourne, Parkville, VIC 3010, Australia. ✉email: tom.karagiannis@monash.edu

who are often unresponsive to current treatments[6]. A number of experimental therapies have shown promising beneficial effects in various models of chronic allergic airways diseases[7–10].

Resveratrol (RV) is a dietary polyphenol found in the skin of red grapes and has been demonstrated to be efficacious in improving airway pathology and function in two different models of chronic allergic airways disease[11,12]. Similarly, L-sulforaphane (LSF), derived from cruciferous vegetables, is known to activate the Nrf2 pathway and have antioxidant and anti-inflammatory properties with potential anti-asthmatic effects[13,14]. Relaxin (RLN) is an anti-fibrotic hormone with pre-clinical potential in the OVA-induced chronic allergic airways models [5,15]. Emerging evidence suggests that histone deacetylase inhibitors (HDACi), such as valproic acid (VPA) and trichostatin A (TSA), can modulate immune responses by skewing the Th1/Th2 balance and activating T-regulatory cell production[16], as well as attenuating chronic allergic airways pathology such as reduced airway constriction induced by methacholine [7], decrease innate inflammatory markers [17] and Th2 response[18]. Evaluating the therapeutic benefits of these experimental compounds in murine OVA-induced models of chronic allergic airways disease are usually done using conventional methodologies such as morphometric histological assessment, immunohistochemistry, or respiratory measurements[10,19–22]. While this approach has been successful, elucidating detailed molecular mechanisms of action has proven more challenging.

Synchrotron Fourier-transform infrared (S-FTIR) microspectroscopy has been used to characterise the mechanism of action of novel therapeutics at the molecular level. The FTIR microspectroscopic technique has been utilised as a diagnostic tool for cancers such as liver[23], lung[24] and ovarian cancer[25], and for kidney stone formation[26]. Furthermore, it has also been used to identify biochemical fingerprints of novel anti-asthmatic therapies such as leaf extracts from *Anacardium occidentale*[27], cromolyn sodium[28], and theophylline[29], and a number of our experimental therapies of interest (Supplementary Table S1).

In this study, we utilised an analytical approach based on the high spatial resolution S-FTIR microspectroscopic technique and principal component analysis (PCA) to investigate the biochemical effects of experimental compounds, RV, VPA, TSA, LSF, and RLN in prevention and reversal models of OVA-induced chronic allergic airways disease. Due to the S-FTIR technique providing a superior spectral quality, in terms of signal to noise ratio, at diffraction-limited spatial resolution for mapping the airways, the time to acquire these maps can be significant. Therefore, we also employed the offline focal plane array–FTIR (FPA-FTIR) imaging technique for a fast acquisition of much larger chemical maps, to enable a broader molecular overview of the surrounding airway tissue. Overall, the aims were to identify key biochemical changes to provide further insights into their mechanism of action, and to correlate our findings with data previously collected in these models using conventional methodologies.

Methods

Animals. Six-week old female BALB/c mice were used to establish the prevention and reversal OVA-induced chronic allergic airways models. These studies complied with the Australian guidelines for the care and use of laboratory animals for scientific purposes and approved by the Monash University animal ethics committee (MARP/2012/085).

Chronic allergic airways disease model. The chronic allergic airways disease model has been previously described[20]. Briefly, control mice ($n=5$) were sensitised with 500 µL of 0.9% saline solution intraperitoneally (IP) (Baxter Health care, New South Wales, Australia). The positive control mice (OVA; $n=5$) and the mice in experimental groups were sensitised with Grade-V OVA (10 µg) (Sigma-Aldrich, MO, USA) with aluminium potassium sulphate adjuvant (400 µg) (AJAX Chemical, Kotara, New South Wales, Australia) diluted in 0.9% saline solution, on days 0 and day 14. Mice were nebulised with OVA for 30 min, three times a week for 6 weeks, from day 21 to day 63. Treatment groups were divided into the prevention and reversal models according to the timelines shown in Fig. 1, and chemical structures of compounds used in the experimental groups are shown in Fig. 2.

Prevention model. Mice were administered (IP) with RV (12.5 mg/kg; $n=2$) (Sigma-Aldrich), VPA (20 mg/ml; $n=2$) (Sigma-Aldrich) or TSA (5 mg/kg; $n=2$) (Sigma-Aldrich) three days per week for six weeks during the OVA nebulisation period, as previously described[20–22]. Mice were euthanised IP with ketamine and xylazine (200 µg/g: 10 µg/g) 4 days after the last nebulisation, on day 67. Lung tissues were removed, fixed with 10% buffered formalin for 24 h before paraffin embedding.

Reversal model. Mice were treated with the indicated compounds on day 64, 24 h after the last OVA nebulisation period. This sub-group of mice were either administered (IP) with LSF (5 mg/kg; $n=3$) (Sigma-Aldrich) five times every 72 h, or daily intranasal (IN) treatment with RLN (0.5 mg/kg/day; $n=3$) (Corthera Inc., San Carlos, CA, USA) for 14 days, as previously described[10]. Mice were euthanised IP with ketamine and xylazine (200 µg/g: 10 µg/g) 24 h after the last treatment, on day 78. Lung tissue was removed, fixed with 10% buffered formalin for 24 h before paraffin embedding.

Sample preparation for FTIR microspectroscopy and histological assessment. Lung samples were sectioned (4 µm in thickness) with a Leica RM 2135 microtome (Leica Biosystems, Wetzlar, Germany) onto either double frosted microscope slides (Mikro-Glass, Australia) for histological assessment or calcium fluoride (CaF_2) windows (Crystan, Dorset, UK) for FTIR microspectroscopy. Samples for FTIR microspectroscopic experiments were deparrafinised by two consecutive 5 min washes with xylene (Sigma-Adrich, Australia), and stored in a desiccator for spectral data collection.

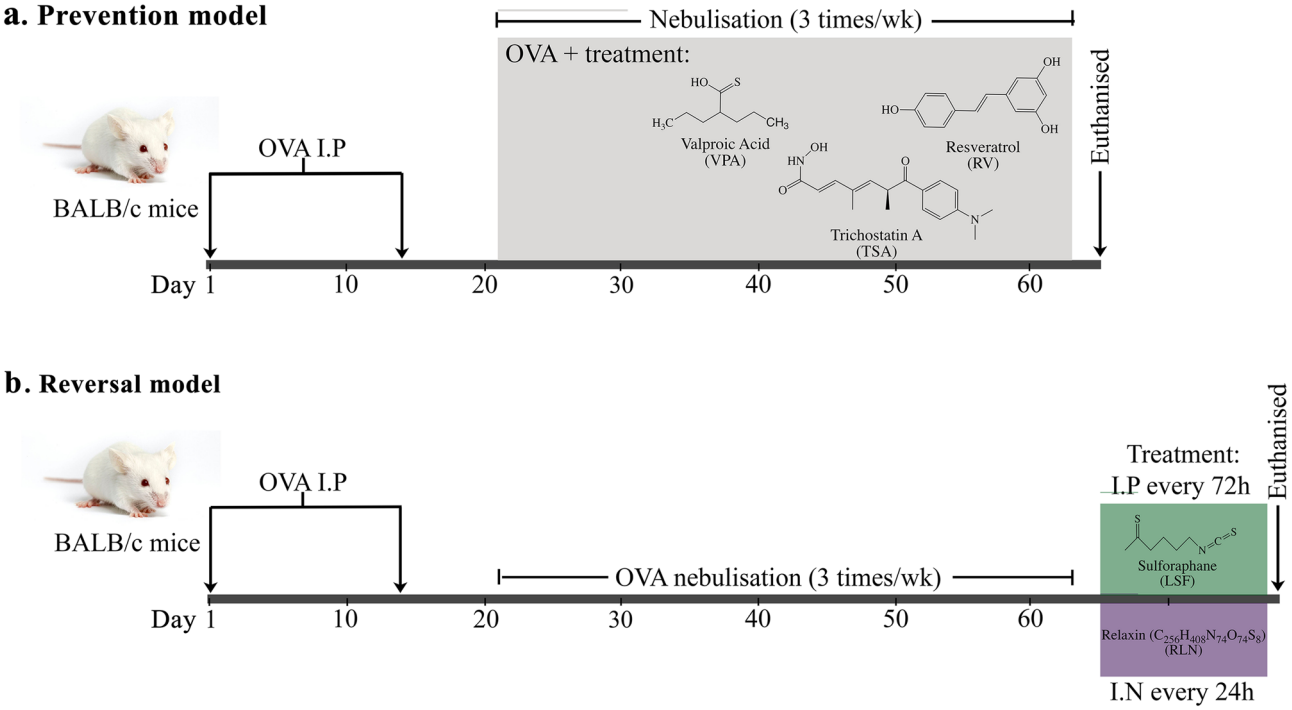

Figure 1. Two murine models of OVA-induced chronic allergic airways timelines. The difference between the prevention **(a)** and reversal **(b)** murine OVA-induced chronic allergic airways model timelines.

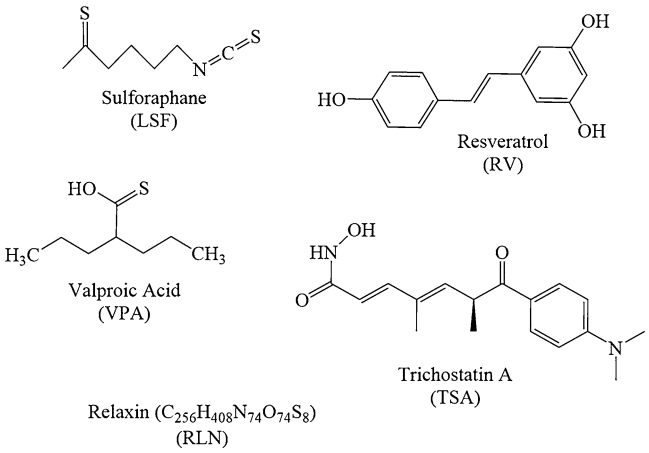

Figure 2. Chemical structure of antioxidant and chromatin modifying compounds.

Focal plane array-Fourier transform infrared (FPA-FTIR) microspectroscopy. All lung tissue sections were imaged using an offline FPA-FTIR microspectroscopic system (Bruker Optik GmbH, Ettlingen, Germany) at the Australian Synchrotron Infrared Microspectroscopy (IRM) Beamline as described earlier[30,31]. Briefly, FPA-FTIR images were acquired in transmission mode with the Bruker Hyperion 3000 FTIR microscope, with a liquid nitrogen cooled 64 × 64 element FPA detector and a matching 15 × objective and condenser (NA = 0.40) coupled to a Bruker Vertex 70 FTIR spectrometer with an internal thermal (Globar) IR source. Each FPA-FTIR image were acquired within the 4,000–800 cm^{-1} spectral region with a sampling area of 180 × 180 μm^2.

The FPA-FTIR spectral images were acquired as previously described[30,31]. Briefly, spectral images were acquired with 8 cm^{-1} resolution, 64 co-added scans, Blackman-Harris 3-term apodisation, Power-Spectrum phase correction, and a zero-filling factor of 2 using the OPUS 7.2 imaging software (Bruker). Furthermore, background control measurements were taken using the same acquisition parameters, by focusing on a clean surface area of the CaF_2 window without any tissue sample.

For the prevention model, 4 × 4 FPA grids were collected from the saline ($n = 5$), OVA ($n = 6$), RV ($n = 1$), TSA ($n = 2$) and VPA ($n = 2$) groups. For the reversal model, FPA-FTIR images were collected for the saline ($n = 5$),

OVA ($n=5$), LSF ($n=2$), and RLN ($n=3$) groups, with the grid sizes collected in either a 4×4 ($n=5$) or 8×8 ($n=9$).

Prior to analysis, all FPA-FTIR images were processed for an atmospheric water correction, followed by baseline correction, vector normalisation and second derivative (25 smoothing points). The spatial distribution of protein on the tissue samples were produced based on integrated areas under the amide I band (1,695–1,600 cm^{-1}). A random selection of at least 50 spectra per image was extracted from the lung epithelium and surrounding tissue and averaged to create an absorbance and inverted second derivative spectra of all the samples.

Synchrotron-FTIR microspectroscopy. The S-FTIR microspectroscopic measurement was performed at the Australian Synchrotron IRM Beamline as previously described[31,32]. Briefly, microspectroscopic measurements were taken in transmission mode using a Bruker Vertex 80v spectrometer coupled with a Hyperion 2000 FTIR microscope (Bruker Optik GmbH, Ettlingen, Germany) and a liquid nitrogen cooled narrow-band mercury cadmium telluride (MCT) detector. The S-FTIR measurement was collected with a $36\times$ IR objective and condenser (NA = 0.50; Bruker Optik GmbH, Ettlingen, Germany) and an aperture size of 5 µm in diameter for every pixel and for every step interval between pixels.

The spectral range of 3,800–700 cm^{-1} using 4 cm^{-1} spectral resolution and 16 co-added scans was utilised for each S-FTIR spectrum. A Blackman-Harris 3-term apodisation, Power-Spectrum phase correction and a zero-filling factor of 2 were utilised as the default acquisition parameters using the OPUS 7.2 software suite (Bruker).

S-FTIR spectral maps of one airway per mouse were acquired from the prevention model including saline ($n=2$), OVA ($n=2$) and RV ($n=2$). For the reversal model, data was acquired for the saline ($n=4$), OVA ($n=3$), LSF ($n=3$), and RLN ($n=3$) groups, with one airway per mouse, with the exception of the saline and OVA groups which had, two airways mapped for two mice, and one mouse, respectively.

Spectral pre-processing and multivariate data analysis. FTIR spectra were first quality-screened using CytoSpec v. 1.4.02 (Cytospec Inc., Boston, MA, USA), to extract and obtain good-quality spectra (> 250 spectra per tissue sample). These spectra were then imported into The Unscrambler 10.1 software package (CAMO Software AS, Oslo, Norway) for PCA. All spectra were transformed into second derivatives using 25-point Savitzky-Golay algorithm to eliminate the broad baseline offset and curvature[33]. The resultant derivative spectra were corrected by extended multiplicative scatter correction (EMSC) method[34] based on biological bands in the spectral regions of 3,063–2,773 cm^{-1} and 1,790–1,018 cm^{-1}. PCA was subsequently performed using the same spectral ranges on the combined datasets, in order to investigate similarities and differences between the tissue groups, and presented in forms of scores and loadings plots[35,36].

Curve fitting analysis. For a comparison of experimental techniques a curve fitting analysis was conducted on the reversal model for the LSF treated mice ($n=3$ per group) S-FTIR maps, and compared to matching lung samples from the histological results of mean-sub-epithelial thickness to compare the different methods for detecting collagen deposition. Briefly, the second inverted second derivative was cut to the spectral region of 1,265–1,990 cm^{-1}, then a new baseline was corrected to the lowest minimum peak of the spectra, and a curve fitting analysis was used based on a Lorentz and Gaussian shape with a maximum of three curves per spectra, to determine the integral of the collagen peak at 1,200 cm^{-1}, using OPUS 7.2 software suite (Bruker).

Statistical analysis. Statistical analysis was performed on the comparison of methods for collagen detection with GraphPad Software Prim v8.0 (San Diego, CA, USA). Results were analysed by a Pearson's correlation analysis. Data was considered statistically significant with a p-value less than 0.05.

Results

FPA-FTIR microspectroscopy. The offline FPA-FTIR microscope provides a general overview of the biochemical fingerprint within the tissue samples. It enables for faster acquisition of larger infrared maps to be taken compared to the higher spectral quality maps obtained from the online S-FTIR. The laboratory-based FPA-FTIR measurement was first performed on all the lung tissue samples to obtain molecular information, specifically the protein distribution, on a much larger area of tissue. The chemical images of the protein distribution based on the amide I band (Fig. 3a, i and b, i) display strong intensity of the protein components in the OVA airway compared to the saline group. In particular, all the treated groups in the prevention model (Fig. 3a, i) exhibit considerably stronger amide I intensities, particularly within the nucleus of epithelial cells, compared to the saline control group. In the reversal group, LSF resembles analogous amide I intensity to the saline control group, while RLN, shows an equivalent level of amide I intensity as those observed for the OVA group (Fig. 3b, i). Furthermore, the chemical image of the LSF group indicates substantially higher peak intensities at 2,956 and 2,872 cm^{-1}, compared to all other treatment groups, indicative of protein acetylation[37].

Comparing the average spectra (Fig. 3a, ii, and b, ii) and the inverted second derivative spectra (Fig. 3a, iii, and b, iii), the position and shape of the amide I and II bands closely resemble the corresponding bands in the saline control groups, suggesting no change in the combination of protein secondary structures in the treated groups.

Synchrotron-FTIR microspectroscopy. The high brightness of the S-FTIR technique results in an enhanced spectral quality in terms of signal to noise (S/N) ratio, which enables acquisition of high-quality FTIR spectra at diffraction-limited spatial resolution. High-quality spectra plays an important role in the accuracy of the subsequent multivariate data analysis results. A summary of the key peaks identified in the S-FTIR results is reported in Table 1.

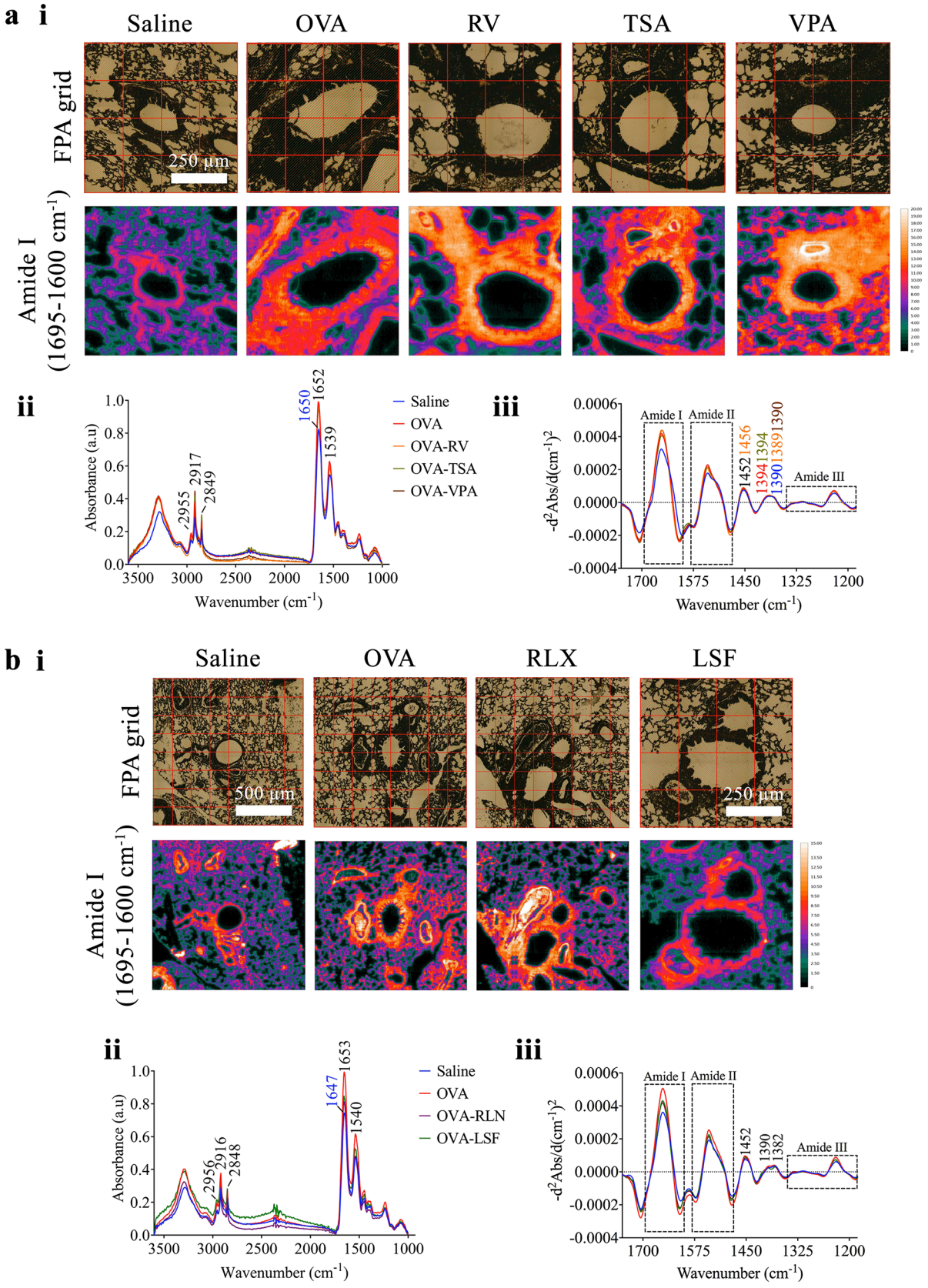

Figure 3. FPA-FTIR chemical images of protein distribution and average absorbance spectra obtained from the two models of allergic airways disease. The chemical images of the prevention model **(a)** and the reversal model **(b)** were produced based on integrated areas under inverted second derivate spectra for amide I band (1,695–1,600 cm^{-1}) (i). A number of spectra were randomly selected from each image (> 50 spectra) to obtain the average absorbance (ii) and inverted second derivative (iii) spectra.

Wavenumber (cm^{-1})	Band assignment
2,872 & 2,960	CH_3 acetylation
2,849 & 2,917	CH_2 propionylation
1,695–1,600	Amide I
1,543	Amide II
1,456	$\delta_{as}(CH_3)$ and $\delta(CH_2)$ vibrations
1,350–1,180	Amide III region
1,379	$\delta(CH_3)$
1,293	Either N–H thymine, of deformation of N–H cytosine
1,236	PO_2^- asymmetric stretching of nucleic acids
1,180	CH_2 stretching
1,200	Collagen
1,088	$\nu_s(PO_2^-)$ stretching

Table 1. Summary of key peaks and their corresponding band assignment.

(i) Absorbance spectrum. S-FTIR absorbance spectra observed for the prevention (Fig. 4a, i) and reversal (Fig. 4b, i) models. In the prevention model (Fig. 4a, i), no major variances amongst the experimental groups were observed at the protein acetylation (2,827 and 2,960 cm^{-1}) and propionylation (2,851 and 2,922 cm^{-1}) bands. In the reversal model (Fig. 4b, i), LSF displays highest peak intensity at 2,956 cm^{-1} compared to all the other groups, this was also confirmed in the FPA-FTIR results, however LSF displayed a lower peak intensity than the saline group at 2,875 cm^{-1}. An increase in these peaks 2,956 and 2,875 cm^{-1} was observed, indicative of CH_3 protein acetylation. The LSF treated group also displayed a strong shift to higher wavelength and decrease in band intensity at peaks 2,923 and 2,852 cm^{-1}, indicative of CH_2 protein propionylation.

(ii) Inverted second derivative spectrum. The inverted second derivative spectra reveal subtle peak changes in the spectral features that are not observed on the absorbance spectra. Here, we specifically focused to the amide region (1,700—1,200 cm^{-1}) and further into the amide III region (1,350–1,200 cm^{-1}) which is important for investigating changes in the protein secondary structures.

Within the amide III region of the prevention model (Fig. 4a, ii), the saline group exhibited a peak at 1,335 cm^{-1}, representing α-helical structures typical of type I collagen[38,39]. The OVA and RV group, on the other hand, showed peaks at 1,317, and 1,311 cm^{-1}, respectively, indicative of β-sheets formations[38]. Random coil structures at band peak 1,284 cm^{-1}[38] are observed in the saline and OVA groups, although the OVA group has a decrease in peak intensity. Further, no random coil structures are observed at the 1,284 cm^{-1} for the RV group, or a peak at 1,200 cm^{-1}, which is attributed to collagen[40].

In the reversal model (Fig. 4b, ii), at the band centered at ~ 1,393 cm^{-1}, typical of CH_2 asymmetric bending and COO– stretching of proteins and fatty acids[41], LSF displays a broadening of this band into two peaks, at 1,396 and 1,384 cm^{-1}, which correspond to CH_3 deformation, and stretching of C–O and the deformation of rather C–H and N–H bonds, respectively[42–44]. While, in the amide III region of the reversal model (Fig. 4b, ii), the OVA and RLN treated groups revealed an increase in α-helical structures, while the saline and LSF treated groups had an increase in β-sheet and random coil structures[38]. Further, the LSF group did not have a peak at 1,201 cm^{-1}.

(iii) Principal component analysis. The scores plot in the prevention model displays clear clusters amongst the three experimental groups (Fig. 4a, iv). The initial PCA result displays a representative of one mouse from each experimental group, as each experimental group demonstrated consistency between individual mice (Supplementary Fig. S2). The saline and OVA groups are largely clustered on the negative side of the PC-1 axis, whereas the RV group is clustered further away from the saline control group on the positive side of the PC-1 axis. Since the separation occurred along the PC-1 axis, the difference in molecular composition between these three groups can be examined through the PC-1 loadings plot. The PC-1 loadings (Fig. 4a, iii), which correlates to 49% of the variance, revealed strong negative loadings at 1666 and 1556 cm^{-1}, which correspond to amide I and II bands, respectively, indicating that the major change in the molecular structure among these three groups is due to the protein components. There are also small contributions coming from the minor loadings at 1,196, and 1,088 cm^{-1}, which could be attributed to collagen, and nucleic acid PO_2^-, respectively.

Similarly, the reversal model displays a clear clustering feature amongst all experimental groups in the scores plot (Fig. 4b, iv). Most groups are clustered within the positive side of the PC-1 axis in the scores plot. The variance along the PC-1 axis (43%) (Fig. 4b, iii) is largely attributed to heavily loaded peaks at 1659 and 1626 cm^{-1}, suggesting that the difference in protein conformation is the major cause of the separation. While the saline, LSF- and RLN-treated groups presented proportionally more of protein in α-helical structure (according to the positive loading at 1659 cm^{-1}), the OVA group is likely to possess protein in β-sheet conformation (negative loading at 1626 cm^{-1}) with a small contribution from collagen component (1,198 cm^{-1}). Furthermore, variance along the PC-2 axis (26%) displays a strong separation between the OVA-LSF and OVA treated groups. The major peaks causing this separation are the same peaks causing the separation along the PC-1 axis, as mentioned above. Therefore, this highlights the differences amongst the OVA and OVA-LSF treated groups is amplified due to these peaks, along both the PC-1 and PC-2 loadings.

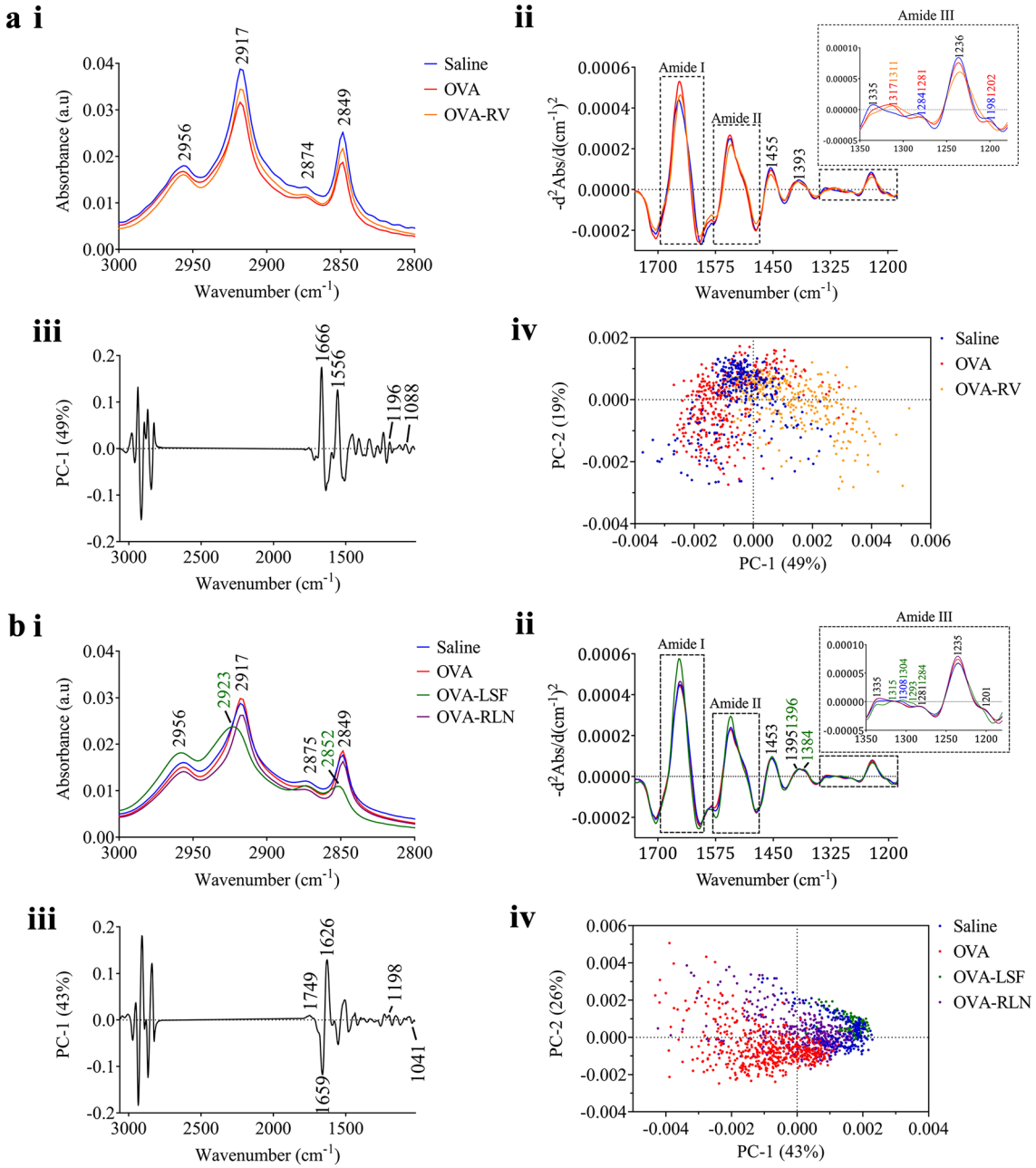

Figure 4. Average S-FTIR spectra and the corresponding PCA analysis obtained from the two models of allergic airways disease. PCA analysis based on S-FTIR spectra of the prevention **(a)** and reversal **(b)** models. The average absorbance (i) and inverted second derivative (ii) spectra obtained from each treatment group, accompanied by the resultant PCA analysis including loadings (iii) and scores (iv) plots.

The key difference observed amongst the prevention and reversal models is the presence of peak 1556 cm^{-1}, as seen in the prevention model loadings plot (Fig. 4a, iii). This band is attributed to α-helices and anti-parallel β-sheets[45].

Comparison between S-FTIR and histology methods for measurement of collagen deposition. A consistent pattern was observed overall between the two methods for collagen detection (Fig. 5). The observed integral of 1,200 cm^{-1}, calculated from a curve fitting analysis, displayed an increased collagen deposition within the OVA control group, consistent with previous observations[20–22], compared to both the saline and LSF treated group, for both conventional histology and S-FTIR methods (Fig. 5a). A Pearson's correlation (Fig. 5b) found a positive correlation ($r = 0.6708$) amongst the two methods and was found to be statistically significant ($p = 0.048$).

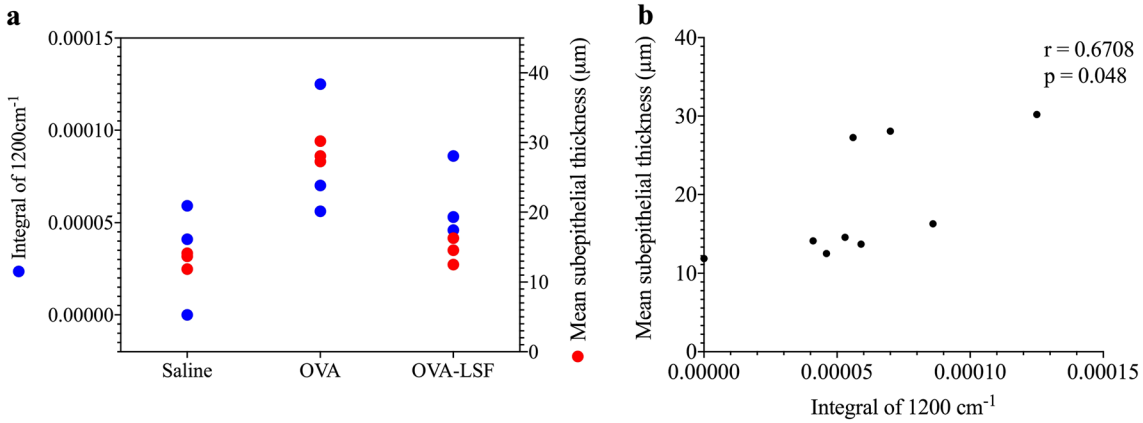

Figure 5. Comparison of collagen presented in the reversal model of allergic airways disease, based on the data obtained from histology (red) and S-FTIR spectra (blue). The mean subepithelial thickness calculated from a Masson's trichrome stain and the integration of band 1,200 cm^{-1} calculated from a curve fitting analysis were used to identify collagen deposition in each method and are plotted together for comparison purposes **(a)**. A Pearson's correlation was performed on the two methods **(b)** and found to have a statistically significant ($p = 0.0479$) positive correlation ($r = 0.6708$).

Discussion

A range of experimental compounds RV, LSF, RLN, VPA and TSA have demonstrated their anti-asthmatic therapeutic potential in well-established chronic allergic airways models[10,19–22]. However, their mechanistic effects remain challenging to distinguish through conventional methods. Henceforth in this study we utilised a novel analytical approach of FPA-FTIR and S-FTIR microspectroscopy to investigate further insights into their mechanism of action, as well as correlate, where possible, these findings to conventional methods.

The S-FTIR microspectroscopy provided us with a better understanding of the key biochemical changes as a result of the different treatments in two variations of the OVA-induced chronic allergic airways murine model. The integration of amide I band, after pre-processing and normalisation of the tissue, highlights that in the prevention model, RV, TSA and VPA led to increased intensities of the amide I band, suggesting an enhanced proportion of protein composition particularly those localised within the nucleus region of epithelial cells[43]. However, it remains unclear why the same was not observed in the reversal model with the LSF treated group compared to the controls.

Previous studies have investigated HDACi in malignant tissue samples using FTIR microspectroscopy to characterise protein acetylation[37,46]. Acetylation is commonly attributed to alterations of CH_3 stretching vibration at 2,872 and 2,960 cm^{-1} and the key band indicative of CH_2 propionylation can also be observed based on the peaks 2,851 and 2,922 cm^{-1}. Our findings indicate an increase in band intensities of the CH_3 stretching band at 2,956 cm^{-1} observed for the LSF treated group, in both the FPA-FTIR and the S-FTIR data, as well as a decrease in the associated CH_2 propionylation bands. One explanation for this effect is likely due to the known chromatin modifying properties of LSF, specifically as an HDACi[47,48]. Our finding are in agreement with Chen and co-workers attributing the intensity and alterations of the CH_3 band to acetylation in their study of HDACi SNDX-275 treated cancer patients in serum samples[37]. However, our prevention model did not indicate an increase in CH_3 stretching band in neither the FPA-FTIR nor S-FTIR data. While RV is a known HDACi[11], factors such as the dose and model used (prevention model) may have had a differential effect on protein acetylation compared to the reversal model. Similarly, Singh and co-workers found that sodium butyrate did not show alterations on the CH_3 acetylation bands, even though it is a known HDACi[46].

The OVA-allergen utilised in our models plays a crucial role in inducing irreversible airway remodeling, a hallmark characteristic of chronic allergic airways disease[21,49,50]. It produces increased epithelial wall thickening, which contributes to airway obstruction and fibrosis and increased collagen deposition surrounding the airways[51–53]. The type of collagen deposition seen in human asthma is largely type I and III, and varies depending on disease severity[54]. Using standard morphometric techniques, some of our previous studies and others have demonstrated that RV, TSA, VPA, RLN and LSF reduced collagen deposition in the airway walls[10,19–22]. However, this approach was unable to differentiate the type of collagen that is modulated by these compounds. Picrosirius red stain can detect the type of collagen deposition but is not routinely measured.

In this study we confirmed that the peak at ~ 1,200 cm^{-1} correlates with collagen deposition, as compared to conventional sub-epithelial thickness measurements, validating this approach. Previous reports have identified characteristic peaks for collagen in biological samples using S-FTIR microspectroscopy (Supplementary Table S3). Both the RV and LSF treated samples showed an analogous absence of the peak at 1,200 cm^{-1} to the saline healthy control group, whereas the OVA group indicated the presence of this peak. Furthermore, in our comparison of S-FTIR at the band 1,200 cm^{-1} and histological staining techniques, our results displayed a positive correlation amongst the two techniques. This suggests the potential application of the S-FTIR technique for semi-quantitative analysis of collagen deposition in the lung tissue with a good correlation to the conventional histological approach. However, it is important to note that the band assignment of 1,200 cm^{-1} is not specific

to the type of collagen present. For the S-FTIR spectra, the type of collagen is typically identified in the amide III region, based on changes in protein secondary structures. Our results suggested type I collagen, typically attributed to α-helical structures at 1,336 cm^{-1}[55], which was increased in the OVA groups, and decreased in the saline and LSF groups. However, this peak may also be attributed to other α-helical-like structures such as heat shock proteins which are also known to be increased in asthma[56]. Furthermore, the saline and LSF treated groups, showed an increase in type III collagen deposition, characterized by an increase in β-sheet formations and random coil structures[57]. Our study indicates the sensitivity of S-FTIR to accurately detect collagen deposition in a similar manner to conventional histology. S-FTIR has the advantage of allowing specific identification the type of collagen.

Allergic inflammation is another major factor that contributes to irreversible remodelling of airway walls and increased bronchial hyperresponsiveness in people with asthma[58–60]. Using conventional methodologies, inflammation is characterised via histological assessment of immune cells infiltrating into airway tissues, changes to the composition of immune cells in bronchoalveolar lavage fluid, and key changes in inflammatory markers[61]. Several reports have identified inflammation by biochemical changes observed through the S-FTIR spectra[62–64]. Based on our data, however, specific peaks characteristic of inflammation were not observed in the acquired S-FTIR spectra. This could be due to the nature of the high spatial resolution of S-FTIR microspectroscopy to insufficiently detect localised inflammation as compared to conventional histology.

It should be emphasized that there were a few peaks presented in the S-FTIR spectra, which are not typically observed through conventional FTIR techniques. These include the peaks at 1,396 and 1,384 cm^{-1}, which were found only in LSF treated group, whereby these peaks were reported to be largely indicative of symmetric CH_3 and C–O stretches, as well as C–H and N–H deformation[65,66]. Furthermore, the peak at 1,236 cm^{-1}, representative of asymmetric stretching vibration of PO^{2-} from nucleic acids[67] was decreased in RV and LSF groups. However, the exact significance of these peaks in the context of chronic allergic airways is yet to be elucidated. These characteristic peaks specific to the S-FTIR microspectroscopic technique may provide further information into their mechanistic actions as potential anti-allergic therapeutics, although will need to be confirmed through conventional techniques.

One of the limitations to the S-FTIR microspectroscopic technique is that the DNA region (below 1,000 cm^{-1}) cannot be detected with the IR spectrum using calcium fluoride transmission windows. This region is of interest, particularly when considering chromatin-modifying compounds, and in future studies alternative transmission windows such as barium fluoride windows could be used to mitigate this limitation. Nevertheless, the technique has provided novel insights into the biochemical changes, independent to the DNA region.

Conclusion

Overall, the application of S-FTIR in combination with offline FPA-FTIR imaging has provided a better understanding of the biochemical changes within complex tissue samples taken from two models of chronic allergic airways disease. The S-FTIR technique enabled detection of changes in collagen deposition, nucleic acids, and protein acetylation. Although these bands may be identified through conventional methodologies including histological assessment and immunofluorescence studies, S-FTIR technique offers an approach to collectively identify these changes in individual maps, with minimal sample preparation required. Further, using S-FTIR numerous novel peaks associated with the experimental compounds were identified. It will be interesting to clarify if these novel peaks are biologically important and mechanistically contribute to potential anti-allergic effects.

Received: 25 October 2019; Accepted: 29 June 2020
Published online: 16 July 2020

References

1. Sagar, S., Akbarshahi, H. & Uller, L. Translational value of animal models of asthma: Challenges and promises. *Eur. J. Pharmacol.* **759**, 272–277 (2015).
2. Wu, Q. *et al.* Regulation of Th1/Th2 balance through OX40/OX40L signalling by glycyrrhizic acid in a murine model of asthma. *Respirology* **21**(1), 102–111 (2016).
3. Kang, S. Y. *et al.* Immunologic regulatory effects of human umbilical cord blood-derived mesenchymal stem cells in a murine ovalbumin asthma model. *Clin. Exp. Allergy* **47**(7), 937–945 (2017).
4. Moldaver, D. M. *et al.* Amelioration of ovalbumin-induced allergic airway disease following Der p 1 peptide immunotherapy is not associated with induction of IL-35. *Mucosal Immunol.* **7**(2), 379–390 (2014).
5. Royce, S. G. *et al.* Serelaxin improves the therapeutic efficacy of RXFP1-expressing human amnion epithelial cells in experimental allergic airway disease. *Clin. Sci. (Lond.)* **130**(23), 2151–2165 (2016).
6. GINA, G.I.f.A. *Global Strategy for Asthma Management and Prevention* (2012).
7. Banerjee, A. *et al.* Trichostatin A abrogates airway constriction, but not inflammation, in murine and human asthma models. *Am. J. Respir. Cell Mol. Biol.* **46**(2), 132–138 (2012).
8. Han, S. G. *et al.* Effects of H2 relaxin on the expression of Epac in a murine model of chronic asthma. *Zhonghua Yi Xue Za Zhi* **92**(46), 3305–3309 (2012).
9. Lee, H. Y. *et al.* Inhibitory effects of resveratrol on airway remodeling by transforming growth factor-beta/smad signaling pathway in chronic asthma model. *Allergy Asthma Immunol. Res.* **9**(1), 25–34 (2017).
10. Royce, S. G. *et al.* Mesenchymal stem cells and serelaxin synergistically abrogate established airway fibrosis in an experimental model of chronic allergic airways disease. *Stem Cell Res.* **15**(3), 495–505 (2015).
11. Gertz, M. *et al.* A molecular mechanism for direct sirtuin activation by resveratrol. *PLoS ONE* **7**(11), e49761 (2012).
12. Alharris, E. *et al.* Resveratrol attenuates allergic asthma and associated inflammation in the lungs through regulation of miRNA-34a that targets FoxP3 in mice. *Front. Immunol.* **9**, 2992 (2018).
13. Duran, C. G. *et al.* A proof-of-concept clinical study examining the NRF2 activator sulforaphane against neutrophilic airway inflammation. *Respir Res.* **17**(1), 89 (2016).

14. Fahey, J. W. & Talalay, P. Antioxidant functions of sulforaphane: A potent inducer of phase II detoxication enzymes. *Food Chem. Toxicol.* **37**(9–10), 973–979 (1999).
15. Royce, S. G. *et al.* Intranasally administered serelaxin abrogates airway remodelling and attenuates airway hyperresponsiveness in allergic airways disease. *Clin. Exp. Allergy* **44**(11), 1399–1408 (2014).
16. Soria-Castro, R. *et al.* Exploring the drug repurposing versatility of valproic acid as a multifunctional regulator of innate and adaptive immune cells. *J. Immunol. Res.* **2019**, 9678098 (2019).
17. Toki, S. *et al.* The histone deacetylase inhibitor trichostatin A suppresses murine innate allergic inflammation by blocking group 2 innate lymphoid cell (ILC2) activation. *Thorax* **71**(7), 633–645 (2016).
18. Choi, J. H. *et al.* Trichostatin A attenuates airway inflammation in mouse asthma model. *Clin. Exp. Allergy* **35**(1), 89–96 (2005).
19. Park, J. H. *et al.* Sulforaphane inhibits the Th2 immune response in ovalbumin-induced asthma. *BMB Rep.* **45**(5), 311–316 (2012).
20. Royce, S. G. *et al.* Protective effects of valproic acid against airway hyperresponsiveness and airway remodeling in a mouse model of allergic airways disease. *Epigenetics* **6**(12), 1463–1470 (2011).
21. Royce, S. G. *et al.* Resveratrol has protective effects against airway remodeling and airway hyperreactivity in a murine model of allergic airways disease. *Pathobiol. Aging Age Relat. Dis.* https://doi.org/10.3402/PBA.v1i0.7134 (2011).
22. Royce, S. G. *et al.* Effects of the histone deacetylase inhibitor, trichostatin A, in a chronic allergic airways disease model in mice. *Arch. Immunol. Ther. Exp. (Warsz)* **60**(4), 295–306 (2012).
23. Thumanu, K. *et al.* Diagnosis of liver cancer from blood sera using FTIR microspectroscopy: A preliminary study. *J. Biophoton.* **7**(3–4), 222–231 (2014).
24. Wang, X. *et al.* FTIR spectroscopic comparison of serum from lung cancer patients and healthy persons. *Spectrochim. Acta A Mol. Biomol. Spectrosc.* **122**, 193–197 (2014).
25. Grzelak, M. M. *et al.* Diagnosis of ovarian tumour tissues by SR-FTIR spectroscopy: A pilot study. *Spectrochim. Acta A Mol. Biomol. Spectrosc.* **203**, 48–55 (2018).
26. Blanco, F. *et al.* High precision mapping of kidney stones using mu-IR spectroscopy to determine urinary lithogenesis. *J. Biophoton.* **8**(6), 457–465 (2015).
27. Awakan, O. J. *et al.* Anti-inflammatory and bronchodilatory constituents of leaf extracts of *Anacardium occidentale* L. in animal models. *J. Integr. Med.* **16**(1), 62–70 (2018).
28. Yasmeen, S., Riyazuddeen, S. & Qais, F. A. Unraveling the thermodynamics, binding mechanism and conformational changes of HSA with chromolyn sodium: Multispecroscopy, isothermal titration calorimetry and molecular docking studies. *Int. J. Biol. Macromol.* **105**(Pt 1), 92–102 (2017).
29. Trivedi, V., *et al*., Intercalated theophylline-smectite hybrid for pH-mediated delivery. Drug Deliv. Transl. Res. (2018).
30. Zawlik, I. *et al.* FPA-FTIR microspectroscopy for monitoring chemotherapy efficacy in triple-negative breast cancer. *Sci. Rep.* **6**, 37333 (2016).
31. Mazarakis, N. *et al.* Synchrotron-Fourier transform infrared maps of ovalbumin-induced murine chronic allergic airways disease: Correlation with conventional histology. *Hell J. Nucl. Med.* **20**(Suppl), 103–113 (2017).
32. Kolodziej, M. *et al.* Classification of aggressive and classic mantle cell lymphomas using synchrotron Fourier transform infrared microspectroscopy. *Sci. Rep.* **9**(1), 12857 (2019).
33. Savitzky, A. & Golay, M. J. E. Smoothing and differentiation of data by simplified least squares procedures. *Anal. Chem.* **36**(8), 1627–1639 (1964).
34. Kohler, A. *et al.* Extended multiplicative signal correction as a tool for separation and characterization of physical and chemical information in Fourier transform infrared microscopy images of cryo-sections of beef loin. *Appl. Spectrosc.* **59**(6), 707–716 (2005).
35. Vongsvivut, J. *et al.* Synchrotron-FTIR microspectroscopy enables the distinction of lipid accumulation in thraustochytrid strains through analysis of individual live cells. *Protist* **166**(1), 106–121 (2015).
36. Vongsvivut, J. *et al.* FTIR microspectroscopy for rapid screening and monitoring of polyunsaturated fatty acid production in commercially valuable marine yeasts and protists. *Analyst* **138**(20), 6016–6031 (2013).
37. Chen, T. *et al.* Pharmacodynamic assessment of histone deacetylase inhibitors: Infrared vibrational spectroscopic imaging of protein acetylation. *Anal. Chem.* **80**(16), 6390–6396 (2008).
38. Cai, S. & Singh, B. R. A distinct utility of the amide III infrared band for secondary structure estimation of aqueous protein solutions using partial least squares methods. *Biochemistry* **43**(9), 2541–2549 (2004).
39. Nogueira, V. C. *et al.* Comparative study of morphometric and Fourier transform infrared spectroscopy analyses of the collagen fibers in the repair process of cutaneous lesions. *Adv. Wound Care (New Rochelle)* **5**(2), 55–64 (2016).
40. Fujioka, N. *et al.* Discrimination between normal and malignant human gastric tissues by Fourier transform infrared spectroscopy. *Cancer Detect. Prev.* **28**(1), 32–36 (2004).
41. Dreissig, I. *et al.* Quantification of brain lipids by FTIR spectroscopy and partial least squares regression. *Spectrochim. Acta A Mol. Biomol. Spectrosc.* **71**(5), 2069–2075 (2009).
42. Wang, H. P., Wang, H. C. & Huang, Y. J. Microscopic FTIR studies of lung cancer cells in pleural fluid. *Sci. Total Environ.* **204**(3), 283–287 (1997).
43. Gazi, E. *et al.* Applications of Fourier transform infrared microspectroscopy in studies of benign prostate and prostate cancer. A pilot study. *J. Pathol.* **201**(1), 99–108 (2003).
44. Dovbeshko, G. I. *et al.* FTIR spectroscopy studies of nucleic acid damage. *Talanta* **53**(1), 233–246 (2000).
45. Verdonck, M. *et al.* Characterization of human breast cancer tissues by infrared imaging. *Analyst* **141**(2), 606–619 (2016).
46. Singh, B. *et al.* Fourier transform infrared microspectroscopy identifies protein propionylation in histone deacetylase inhibitor treated glioma cells. *J. Biophoton.* **5**(3), 230–239 (2012).
47. Martin, S. L., Kala, R. & Tollefsbol, T. O. Mechanisms for the inhibition of colon cancer cells by sulforaphane through epigenetic modulation of microRNA-21 and human telomerase reverse transcriptase (hTERT) down-regulation. *Curr. Cancer Drug Targets* **18**(1), 97–106 (2018).
48. Myzak, M. C. *et al.* Sulforaphane inhibits histone deacetylase in vivo and suppresses tumorigenesis in Apc-minus mice. *Faseb J.* **20**(3), 506–508 (2006).
49. Royce, S. G., Patel, K. P. & Samuel, C. S. Characterization of a novel model incorporating airway epithelial damage and related fibrosis to the pathogenesis of asthma. *Lab Invest.* **94**(12), 1326–1339 (2014).
50. Kwon, M.-J. *et al.* Superoxide dismutase 3 controls adaptive immune responses and contributes to the inhibition of ovalbumin-induced allergic airway inflammation in mice. *Antioxid. Redox Signal.* **17**(10), 1376–1392 (2012).
51. Agache, I. *et al.* Untangling asthma phenotypes and endotypes. *Allergy* **67**(7), 835–846 (2012).
52. Chung, K. Defining phenotypes in asthma: A step towards personalized medicine. *Drugs* **74**(7), 719–728 (2014).
53. Gibson, P. G. Inflammatory phenotypes in adult asthma: Clinical applications. *Clin. Respir. J.* **3**(4), 198–206 (2009).
54. Chakir, J. *et al.* Airway remodeling-associated mediators in moderate to severe asthma: Effect of steroids on TGF-beta, IL-11, IL-17, and type I and type III collagen expression. *J Allergy Clin. Immunol.* **111**(6), 1293–1298 (2003).
55. Jackson, M. *et al.* Beware of connective tissue proteins: Assignment and implications of collagen absorptions in infrared spectra of human tissues. *Biochim. Biophys. Acta* **1270**(1), 1–6 (1995).
56. Yombo, D.J.K., *et al*. Heat Shock Protein 70 is a positive regulator of airway inflammation and goblet cell hyperplasia in a mouse model of allergic airway inflammation. J. Biol. Chem. (2019).

57. Petibois, C. *et al.* Analysis of type I and IV collagens by FT-IR spectroscopy and imaging for a molecular investigation of skeletal muscle connective tissue. *Anal. Bioanal. Chem.* **386**(7–8), 1961–1966 (2006).
58. Lambrecht, B. N. & Hammad, H. The immunology of asthma. *Nat. Immunol.* **16**(1), 45–56 (2015).
59. Barnes, P. J. Cellular and molecular mechanisms of chronic obstructive pulmonary disease. *Clin. Chest Med.* **35**(1), 71–86 (2014).
60. Fahy, J. V. Type 2 inflammation in asthma—Present in most, absent in many. *Nat. Rev. Immunol.* **15**(1), 57–65 (2015).
61. Germolec, D. R. *et al.* Markers of inflammation. *Methods Mol. Biol.* **1803**, 57–79 (2018).
62. Wiercigroch, E. *et al.* FT-IR spectroscopic imaging of endothelial cells response to tumor necrosis factor-alpha: To follow markers of inflammation using standard and high-magnification resolution. *Anal. Chem.* **90**(6), 3727–3736 (2018).
63. Tosi, G. *et al.* FTIR microspectroscopy of melanocytic skin lesions: A preliminary study. *Analyst* **135**(12), 3213–3219 (2010).
64. Eto, M. *et al.* Glycogen synthase kinase-3 mediates endothelial cell activation by tumor necrosis factor-alpha. *Circulation* **112**(9), 1316–1322 (2005).
65. Wang, X. Q. *et al.* Sphingosylphosphorylcholine induces α-smooth muscle actin expression in human lung fibroblasts and fibroblast-mediated gel contraction via S1P2 receptor and Rho/Rho-kinase pathway. *Prostaglandins Other Lipid Mediat.* **108**, 23–30 (2014).
66. Zohdi, V. *et al.* Importance of tissue preparation methods in FTIR micro-spectroscopical analysis of biological tissues: "Traps for new users". *PLoS ONE* **10**(2), e0116491 (2015).
67. German, M. J. *et al.* Characterization of putative stem cell populations in the cornea using synchrotron infrared microspectroscopy. *Invest. Ophthalmol. Vis. Sci.* **47**(6), 2417–2421 (2006).

Acknowledgements

TCK and the Epigenomic Medicine Laboratory (Central Clinical School, Monash University) are in part supported financially and intellectually by McCord Research (Iowa, USA). PVL is a NHMRC CDF2 recipient. NM is supported by Australian Government Research Training Program Scholarship. Synchrotron IR Microspectroscopy and focal plane array FTIR imaging were undertaken at the IRM beamline at the Australian Synchrotron, part of ANSTO.

Author contributions

T.C.K. and S.G.R. conceived and planned the overall study. S.G.R. and C.S.S. coordinated the animal models and N.M. and K.V. prepared the samples and acquired the maps at the Australian Synchrotron. J.V., K.R.B. and M.J.T. contributed to the utilisation of the S-FTIR beamline at the Australian Synchrotron. N.M. analysed the data, with the support of JV, and produced the draft of the manuscript. J.V., K.J.S., P.V.L., and T.C.K. contributed equally to iterations of editing the manuscript.

Competing interests

Epigenomic Medicine Laboratory (Central Clinical School, Monash University) (TCK) is in part supported financially by McCord Research (Iowa, USA), which has a commercial interest in sulforaphane. PVL, KRB, MJT, KV, JV, SGR, CSS, KJS and NM have no competing interests.

Additional information

Supplementary information is available for this paper at https://doi.org/10.1038/s41598-020-68671-2.

Correspondence and requests for materials should be addressed to T.C.K.

Reprints and permissions information is available at www.nature.com/reprints.

Publisher's note Springer Nature remains neutral with regard to jurisdictional claims in published maps and institutional affiliations.